analytical chemistry

Letter

Cite This: Anal. Chem. 2019, 91, 9371−9375

pubs.acs.org/ac

Coherent Raman Scattering Unravelling Mechanisms Underlying Skull Optical Clearing for Through-Skull Brain Imaging

Yage Chen,[†,#,‡] Shaojun Liu,[†,#,‡] Hongji Liu,[⊥,‡] Shen Tong,[⊥,‡] Huajun Tang,[†,#] Chao Zhang,[†,#] Shuai Yan,[†,#] Haozheng Li,[†,#] Guang Yang,[†,#] Dan Zhu,[*,†,#] Ke Wang,[*,⊥] and Ping Wang[*,†,#]

[†]Britton Chance Center for Biomedical Photonics, Wuhan National Laboratory for Optoelectronics-Huazhong, University of Science and Technology, Wuhan, Hubei 430074, China

[#]MoE Key Laboratory for Biomedical Photonics, Collaborative Innovation Center for Biomedical Engineering, School of Engineering Sciences, Huazhong University of Science and Technology, Wuhan, Hubei 430074, China

[⊥]Key Laboratory of Optoelectronic Devices and Systems of Ministry of Education and Guangdong Province, College of Physics and Optoelectronic Engineering, Shenzhen University, Shenzhen, Guangdong 518060, China

Supporting Information

ABSTRACT: Optical access of a mouse brain using microscopes is the key to study brain structures and functions in vivo. However, the opaque skull of a mouse has to be either opened or thinned in an invasive way to attain an adequate imaging depth in the brain. Mild skull optical clearing is highly desired, but its chemical mechanism is far from being understood. Here, we unraveled the molecular process underlying optical clearing of the mouse skull by label-free hyperspectral stimulated Raman scattering (SRS) microscopy, thereby discovering the optimal clearing strategy to turn a turbid skull into a transparent skull window. Furthermore, we demonstrated in vivo three-photon imaging of vascular structures as deep as 850 μm in the cortex of the mouse brain. Coherent Raman based microspectroscopy holds great promise to advance skull and tissue clearing methods in the future.

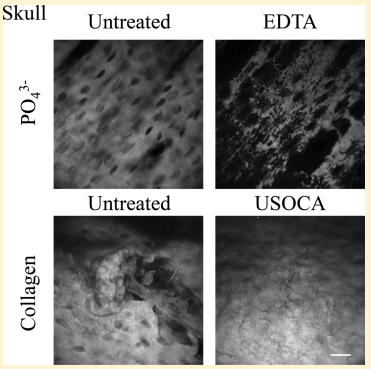

To achieve in vivo brain imaging by optical microscopes, the skull of a mouse is typically opened or thinned to avoid serious optical scattering and aberrations.[1−3] However, neither of them is technically easy to perform on a live mouse. Especially, the invasive skull operations can result in physiological alternations, which may interfere with the brain functions and cause unknown side effects to the live mouse.[4,5] Noninvasive through-skull imaging has been explored recently.[6] By reducing the roughness of the skull surface via index-matching glue, three-photon excitation was able to reach an imaging depth >500 μm in the mouse brain.[7] As an alternative technique, skull optical clearing with safe and easy-handling agents can improve skull transparency for direct brain imaging.[8−12] At a depth of about 250 μm in the brain cortex, the two-photon microscope observed clear microvasculatures and cortical structures at synaptic resolution.[13] Also, the optical clearing skull window could be repeatedly established from the regional parietal bone to the bihemisphere.[14] In fact, the decalcification of the inorganic mineral hydroxyapatite and the depolymerization of collagens are involved in the skull clearing strategies.[15] However, the exact chemical processes happening between the bone and the various optical clearing agents are not really observable and clear. It is because the high-resolution imaging tools with chemical specification are not readily available. Here, we show that hyperspectral stimulated Raman scattering (SRS) microscopy[16−19] is capable of visualizing the major chemical compositions of the skull and monitoring their spatial alternations in concentration during the skull clearing process. With quantitative imaging, we developed effective optical clearing strategy, which turned the turbid mouse skull into a transparent visual window (visible and NIR) for multiphoton imaging.

To visualize the three-dimensional (3D) microstructures of the skull, we performed hyperspectral SRS imaging of the mouse skull and acquired the Raman spectra at all pixels of the images for in situ chemical identification (Figure S1). Figure 1a and Figure S2a show the chemical images of the collagenous fibers in the skull surface, and Figure 1b illustrates the Raman spectrum obtained in the indicated location (colored in dark green). We found that the Raman band of type I collagen[20] at 2 950 cm^{-1} (⑥) was shifted from the typical protein band at 2 930 cm^{-1} (e.g., bovine serum albumin (BSA), colored in light green). Among the collagenous fibers, we also spotted lipid droplets with a size less than 2 μm (colored in magenta). Interestingly, these scattered lipid droplets exhibited a distinct Raman band at 2 882 cm^{-1} (⑤, Figure 1b), which implied that they were saturated fat.[21] In contrast, the typical unsaturated fat, glyceryl trioleate (TO), presented a characteristic Raman

Received: June 8, 2019
Accepted: July 24, 2019
Published: July 24, 2019

DOI: 10.1021/acs.analchem.9b02624
Anal. Chem. 2019, 91, 9371−9375

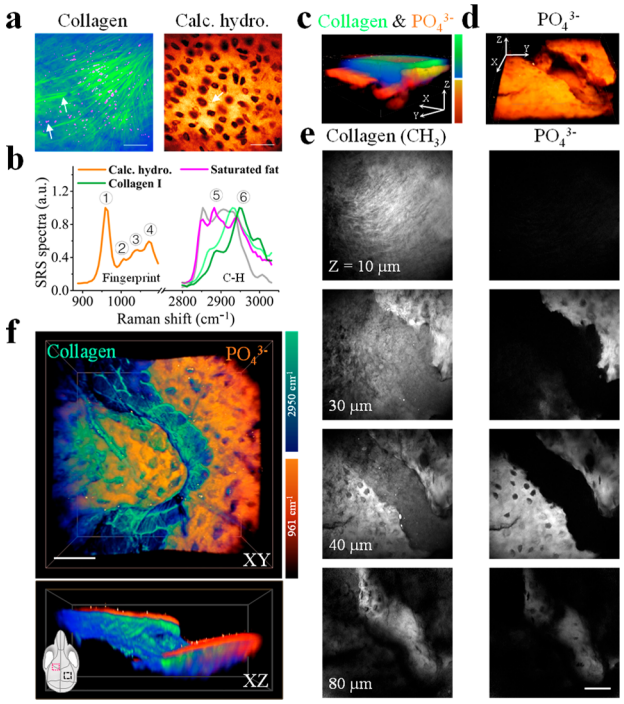

Figure 1. Hyperspectral SRS imaging of 3D microstructures in the mice skull. (a) The SRS images of collagenous fibers and calcium hydroxyapatite (Calc. hydro.). (b) SRS spectra obtained from the indicated locations in part a. The characteristic Raman bands: $\nu_1PO_4^{3-}$ of hydroxyapatite at 961 cm^{-1}, benzene rings of protein at 1 005 cm^{-1}, $\nu_3PO_4^{3-}$ at 1 040 cm^{-1}, and $\nu_1CO_3^{2-}$ of carbonate at 1 073 cm^{-1} (①, ②, ③, and ④, orange), lipid droplets at 2 882 cm^{-1} (⑤, magenta), type I collagen at 2 950 cm^{-1} (⑥, dark green), BSA at 2 930 cm^{-1} (light green), and glyceryl trioleate (gray). (c,d) Quantitative 3D images of both collagen and calcium hydroxyapatite in the coronal suture of the skull. Collagen and PO_4^{3-} (c) and PO_4^{3-} (d). (e) 2D imaging at depths of Z = 10, 30, 40, 80 μm of the skull. (f) 3D structures of the suture of another skull, in which the gap between the two bone lamellas was not fully ossified by hydroxyapatite. The cranium bones were obtained from the red-boxed region of indicated in part f. Scale bars, 50 μm.

band at both 2 850 cm^{-1} (CH_2) and 3 007 cm^{-1} (=CH) (gray in Figure 1b).

The other major chemical compositions of the skull are calcium hydroxyapatite and carbonate.[22] Thus, we performed molecular imaging of the mineral part beneath the collagenous fibers (Figure 1a, right) and explored their SRS spectra in the fingerprint region of Raman (orange in Figure 1b). Interestingly, the bone consisted of a high density of bone lacunae, and some of them were occupied by osteocytes (Figure S2b). In the indicated location, the SRS spectrum presented rich vibrational features of bone, including $\nu_1PO_4^{3-}$ of hydroxyapatite band at 961 cm^{-1}, $\nu_3PO_4^{3-}$ at 1 040 cm^{-1}, and $\nu_1CO_3^{2-}$ of B-type carbonate at 1 073 cm^{-1} (Figure 1b, ①, ③, and ④).[23,24] The SRS spectrum of bone also displayed a special Raman band at 1 005 cm^{-1} (②), which is the breathing mode of benzene rings contained in amino acids in proteins.[25,26] Thus, it implied that a large number of proteins grew with calcium hydroxyapatite in the skull. In further investigation, we conducted quantitative 3D imaging of both collagen and calcium hydroxyapatite in the coronal suture of the skull. The SRS microscope presented unique advantages in chemical specification and optical sectioning to image distinct biomolecules in bone. Figure 1c shows the 3D structure of a piece of coronal suture of the mouse skull. We found that the collagenous fibers were mainly distributed on the top of the skull and symbiotic with the framework built by calcium hydroxyapatite (Figure 1c,d and Movie S1). Figure 1e presents the concentration maps of collagen and calcium hydroxyapatite at different depths of the skull. Figure 1f shows the 3D structures of the suture of another skull, in which the two bone lamellas were not fully ossified by hydroxyapatite[27] (Figure S3). As a result, the collagens played an essential role to fill the gap and ensured the complete seal of the skull.

After we proved the capability of SRS microscopy for 3D chemical imaging of the mouse skull, we examined the process of optical clearing with chemical agents, including collagenase, ethylenediaminetetraacetic acid disodium solution (abbreviated as EDTA), and the chemical combination of urea,[28,29] ethanol, sodium hydroxide (NaOH), and dodecylbenzenesulfonate acid (together termed as USOCA).[14] Figure 2a–c chemically illustrates the microstructural variations of collagen fibers and hydroxyapatite at depths of 15 and 40 μm as collagenase and EDTA were applied to the skull surface, sequentially. Meanwhile, the sectional views of the skull depict the compositional variations along the skull depth. At the surface of the skull, the dominated tissue composition was collagen fibers. Beneath the layer of collagen fibers, the proteins and hydroxyapatite were organized closely to form the main structure of the skull (Figure 2a). After treatment of 10% collagenase on the surface of the skull for 5–10 min, we observed that the collagen fibers on the surface were depolymerized effectively (Figure 2b, left, Z = 15 μm). However, the collagenase was not able to degrade hydroxyapatite and collagens embedded in hydroxyapatite (Figure 2b, Z = 40 μm). Furthermore, we briefly cleaned collagenase and replaced it with 10% EDTA, which is able to sequester Ca^{2+} in hydroxyapatite and thus weakens the microstructure of the bone.[30] As shown in Figure 2c, we directly visualized hydroxyapatite corruption appearing in the same location of the skull (detailed images in Figure S4a and Movie S2). Because of the bone disintegration, a large number of cavities formed around the bone lacunae only after 5–10 min of EDTA immersion (Figure 2c, PO_4^{3-}, Z = 40 μm). At a depth of 30 μm, almost all hydroxyapatite has been degraded (Figure S4a). In the sectional view shown in Figure 2c, we found that the thickness of the hydroxyapatite in the skull was significantly reduced from the original position of ~15 μm to ~40 μm (repeated experiments in Figure S4b,c). Importantly, the spatial distribution of collagens became more homogeneous and the SRS images of the original lacunae became more clear (Figure 2c, left). It implies that EDTA cannot only disintegrate hydroxyapatite but also homogenizes the proteins and realizes great transparency of the skull. Meanwhile, the collagen layers maintained the original thickness and thus actually preserved the integrity of the skull.

USOCA is recognized as another type of optical clearing agent for adult mouse skull.[14] The major compositions, ethanol solution of urea (S1), can rapidly depolymerize the triple helix of collagens,[29,31] and the NaOH solution of dodecylbenzenesulfonate (S2) is able to homogenize the collagens.[32] In the control experiment (Figure 2d, left), the collagens on the surface of the skull were highly inhomogeneous. After we treated the mouse skull with USOCA only for 15 min, the proteins in both the surface and deep zones of the skull were depolymerized and redistributed homogeneously (Figure 2e (left), Figure S5 and Movie S3). We noticed the weak SRS

DOI: 10.1021/acs.analchem.9b02624
Anal. Chem. 2019, 91, 9371–9375

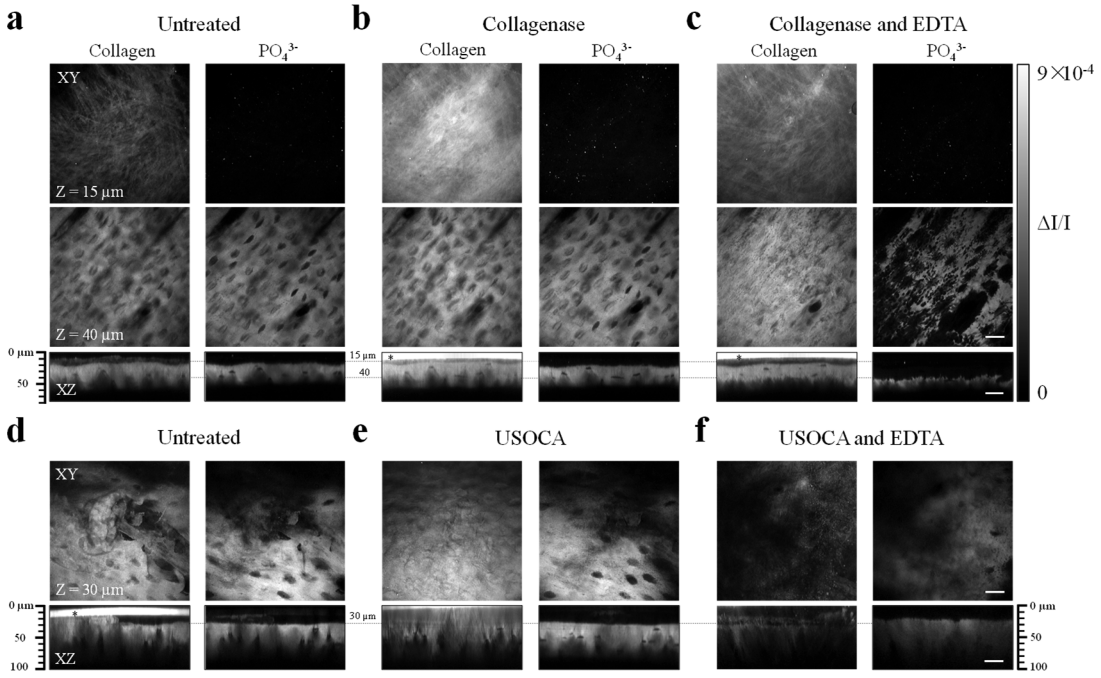

Figure 2. 3D SRS images of skull optical clearing process. (a–c) Microstructural images of collagenous fibers and hydroxyapatite in a piece of parietal bone from an 18-day-old mouse. The skull was untreated (a), treated with 10% collagenase for 5–10 min (b), and treated with 10% EDTA for 5–10 min (c), successively. (d–f) Microstructural variations of collagenous fibers and hydroxyapatite in parietal bones from 2-month-old mice. The bone before treatment (d), treatment of USOCA for 15 min (e), and then treatment of 10% EDTA for 5–10 min on another bone (f). The cranium bones were from parietal regions of the skull, which is boxed in black in Figure 1f. The asterisks (*) indicate the locations of the plastic films that covered the samples, which presented strong SRS signals. Scale bars, 30 μm.

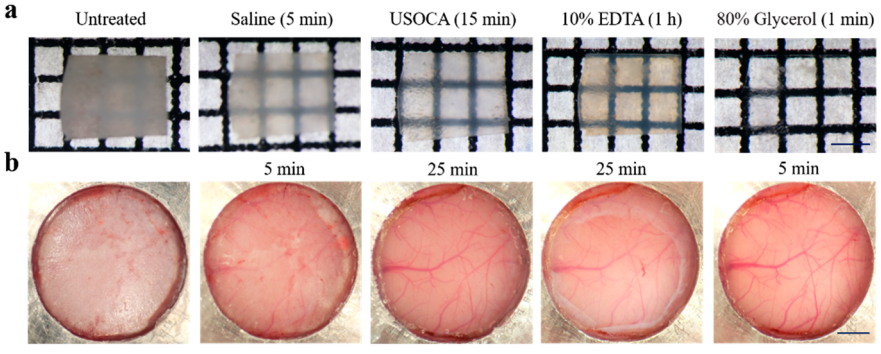

Figure 3. Bright-field images of the skull before and after optical clearing. (a) In vitro images of a piece of parietal bone from a 2-month-old mouse. The bone was successively immersed in saline for 5 min, USOCA for 15 min, 10% EDTA for 1 h, and 80% glycerol for 1 min. (b) In vivo images of mouse brain after skull optical clearing. Exposed skull of the mouse was photographed before and after successive treatment of saline for 5 min, USOCA for 25 min, 10% EDTA for 25 min, and 80% glycerol for 5 min (similar results for $n > 5$). Scale bars, 1.5 mm (a) and 1 mm (b).

signal from USOCA on the surface of the skull, but this background interference became a minimum in the deep region of the skull (Figure S6b).[18,28,33,34] It suggests that the USOCA has stronger capability to dissolve the proteins in contrast to collagenase. As a result, the skull appeared more transparent, and the SRS images of osteocytic lacunae in the same location of hydroxyapatite displayed much clearer shapes in contrast to the control (Figure 2d,e, right). Furthermore, we tested another skull, which was sequentially treated with USOCA and EDTA before. Strikingly, we found that the densities of both collagens and hydroxyapatite were significantly reduced, while the depths of them remained roughly the same. It was probably because the corrosivity of EDTA became mild in the presence of USOCA. Hence, the reduced density of proteins and minerals in the skull can significantly mitigate the light distortion, which is highly preferred for the through-skull imaging. Meanwhile, the skull maintained with thick and homogenized proteins and hydroxyapatite could effectively protect the brain from outside environments.

Further, we compared the skull transparency after we treated the mouse skull with saline, USOCA, EDTA, and glycerol sequentially. As shown in Figure 3a,b, the untreated skulls were almost opaque. After treatment by a simple saline immersion for 5 min, the skulls became translucent. After the optical clearing treatment of USOCA for 15 min, the in vitro skull was no longer turbid. In addition, for in vivo treatment of USOCA for 25 min, the skull turned to be transparent, and we could directly visualize the major brain blood vessels beneath the skull. Next, we applied 10% EDTA to the skulls for 1 h (in vitro) and 25 min (in vivo) to degrade the hydroxyapatite, respectively. However, both skulls returned to be turbid. Importantly, the in vitro skull became remarkably transparent

DOI: 10.1021/acs.analchem.9b02624
Anal. Chem. 2019, 91, 9371–9375

in less than 1 min as we treated the skull with 80% glycerol. We also discovered that the original rigid skull turned to be very soft and flexible as a transparent plastic film. The in vivo test also confirmed the great skull transparency achieved with sequential treatment of USOCA, EDTA, and glycerol (Figure 3b). More cortical blood vessels and their detailed branches were visually observable. Although glycerol can improve the transparency of the skull by matching the refraction index,[35] we found that EDTA indeed played an essential role in this clearing process and must be used before applying glycerol. To confirm this, we reversed the procedure and treated the skull with glycerol before EDTA. We found that the optical clearing was not effective (Figure S7), which probably implied that glycerol may reduce the corrosive power of EDTA. Furthermore, we performed a safety assessment of this method. The result of hematoxylin and eosin (H&E) staining of a brain slice showed no difference between the untreated and treated regions. It indicates that this optical clearing technique does not affect the microenvironment (Figure S8).

Next, we performed three-photon fluorescence imaging of the vasculature in the mouse brain in vivo (Figure 4a). Through the cleared skull (Figure 4b), the 3D reconstructed image clearly reveals the Texas Red-labeled brain vasculature in the 2-month-old mouse. As shown in Figure 4a, the thickness of the skull after optical clearing was maintained at about 100 μm, and "0" denotes the surface of the brain. From the individual 2D images and z-projections of the substack shown in Figure 4c, blood vessels down to a depth of 850 μm were still visible. This indicates that our skull clearing technique is suitable for through-the-skull deep-brain multiphoton microscopy. Although the transparency of the cleared skull is high, we postulate that the current imaging depth could be partly limited by the flatness of the cleared skull, which is bound to introduce aberrations to the wavefront of the laser and degrades the laser focus, especially deep in the brain.

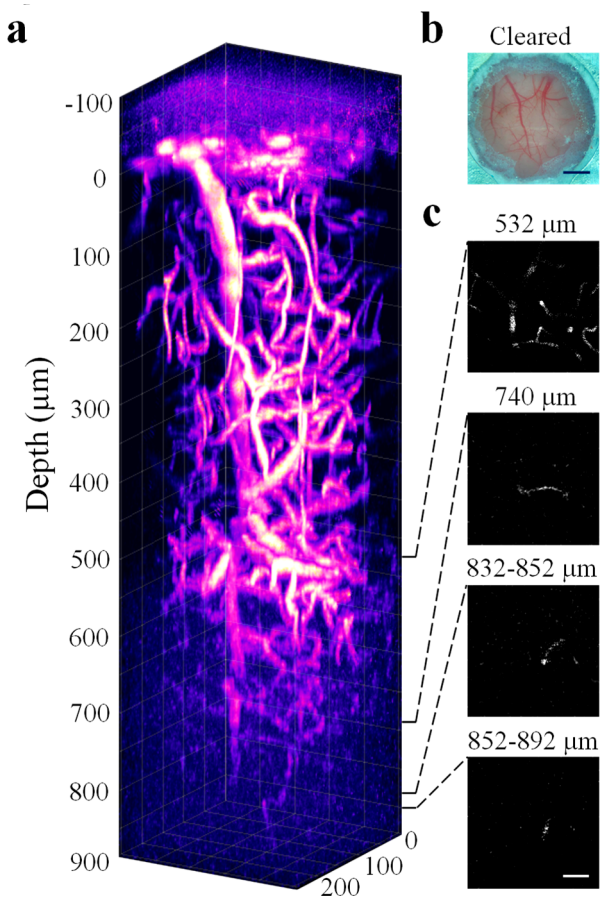

Figure 4. Three-photon excitation imaging of mouse vasculature through the transparent skull window. (a) 3D reconstruction of the vasculature of the mouse brain with Texas Red-labeled (BALB/c mouse, 26 g, 8 weeks old; similar results for $n = 3$). (b) Photographed image of the mouse skull after optical clearing. (c) Three-photon excitation images at various depths. Scale bars, 1 mm (b) and 50 μm (c).

In summary, we implemented a hyperspectral SRS microscope to directly visualize the optical clearing process of a mouse skull. The high-resolution and label-free 3D imaging not only revealed spatial distributions of collagens and mineral hydroxyapatite in the skull but also uncovered chemical and microscopic processes of their transition to form a transparent skull window. We found that USOCA, EDTA, and glycerol played different roles during skull optical clearing. USOCA only degrades the protein-rich composition, mainly collagenous fibers on surface of the skull and proteins embedded in the bone. EDTA is able to homogenize the proteins and effectively decompose the matrix of inorganic phosphates by chelating the calcium ions and significantly reduces both the thickness and density of inorganic minerals in the skull. Importantly, USOCA must be used first to reduce the corrosivity of EDTA. As a result, the combination of USOCA and EDTA could reduce the density of both the organic and inorganic compositions of the bone but maintain the thickness of the skull. The index-matching glycerol should be applied in the last step to achieve the best transparency of the skull. We further demonstrated that the three-photon microscope was able to image the cortical vasculature at a depth of >850 nm beneath the transparent skull window. The developed skull visual window may open the possibilities for less invasive in vivo brain imaging. Assisted by mathematical simulation of the photon scattering in different materials,[15] this molecular 3D imaging methodology holds great promise to lead to advanced tissue clearing techniques in the future.

■ ASSOCIATED CONTENT

Supporting Information

The Supporting Information is available free of charge on the ACS Publications website at DOI: 10.1021/acs.analchem.9b02624.

Methods; Figure S1, schematic of hyperspectral SRS apparatus; Figure S2, supporting data for Figure 1a; Figure S3, 3D distributions of collagen and calcium hydroxyapatite in another skull suture; Figures S4 and S5, SRS images of the skull at different depths with treatment of EDTA and USOCA, respectively; Figure S6, SRS spectra of collagenase, EDTA, and USOCA; Figure S7, optical clearing test with reversed sequence of EDTA and glycerol treatments; and Figure S8, safety assessment of optical clearing skull window (PDF)

Movie S1, 3D distributions of collagen and hydroxyapatite in suture of mouse skull (Figure 1c,d)(AVI)

Movie S2, 3D SRS imaging of microstructural variations of hydroxyapatite before and after treatment with EDTA in parietal bone from an 18-day-old mouse (Figure 2a,c) (AVI)

DOI: 10.1021/acs.analchem.9b02624
Anal. Chem. 2019, 91, 9371−9375

Movie S3, 3D SRS imaging of collagen before and after treatment with USOCA in parietal bone from a 2-month-old mouse (Figure 2d,e) (AVI)

AUTHOR INFORMATION

Corresponding Authors

*E-mail: p_wang@hust.edu.cn.
*E-mail: dawnzh@hust.edu.cn.
*E-mail: kewangfs@szu.edu.cn.

ORCID

Yage Chen: 0000-0002-6601-5198
Shuai Yan: 0000-0002-9083-7749
Ke Wang: 0000-0002-9445-2168
Ping Wang: 0000-0002-5168-6829

Author Contributions

‡Y.C., S.L., H.L., and S.T. contributed equally.

Notes

The authors declare no competing financial interest.

ACKNOWLEDGMENTS

P.W. acknowledges the supports from the National Key Research and Development Program of China (Grant 2016YFA0201403), the National Natural Science Foundation of China (Grant 61675075), the Chinese Recruitment Program of Global Experts, and the Director Fund of the Wuhan National Laboratory for Optoelectronics. D.Z. is funded by National Natural Science Foundation of China (Grants 91232710 and 31571002) and the Science Fund for Creative Research Group of China (Grant 61421064). K.W. is supported by the National Natural Science Foundation of China (Grant 61775143) and the Key Project of Department of Education of Guangdong Province (Grant 2017KZDXM073).

REFERENCES

(1) Holtmaat, A.; Bonhoeffer, T.; Chow, D. K.; Chuckowree, J.; De Paola, V.; Hofer, S. B.; Hubener, M.; Keck, T.; Knott, G.; Lee, W. C. A.; Mostany, R.; Mrsic-Flogel, T. D.; Nedivi, E.; Portera-Cailliau, C.; Svoboda, K.; Trachtenberg, J. T.; Wilbrecht, L. *Nat. Protoc.* **2009**, *4* (8), 1128−1144.
(2) Yang, G.; Pan, F.; Parkhurst, C. N.; Grutzendler, J.; Gan, W. B. *Nat. Protoc.* **2010**, *5* (2), 201−208.
(3) Drew, P. J.; Shih, A. Y.; Driscoll, J. D.; Knutsen, P. M.; Blinder, P.; Davalos, D.; Akassoglou, K.; Tsai, P. S.; Kleinfeld, D. *Nat. Methods* **2010**, *7* (12), 981−984.
(4) Xu, H. T.; Pan, F.; Yang, G.; Gan, W. B. *Nat. Neurosci.* **2007**, *10* (5), 549−551.
(5) Dorand, R. D.; Barkauskas, D. S.; Evans, T. A.; Petrosiute, A.; Huang, A. Y. *Intravital* **2014**, *3* (2), No. e29728.
(6) Park, J. H.; Sun, W.; Cui, M. *Proc. Natl. Acad. Sci. U. S. A.* **2015**, *112* (30), 9236−9241.
(7) Wang, T.; Ouzounov, D. G.; Wu, C.; Horton, N. G.; Zhang, B.; Wu, C. H.; Zhang, Y.; Schnitzer, M. J.; Xu, C. *Nat. Methods* **2018**, *15* (10), 789−792.
(8) Silasi, G.; Xiao, D. S.; Vanni, M. P.; Chen, A. C. N.; Murphy, T. H. *J. Neurosci. Methods* **2016**, *267*, 141−149.
(9) Tuchin, V. V. *Optical Clearing of Tissues and Blood*; SPIE Press: Bellingham, WA, 2006.
(10) Genina, E. A.; Bashkatov, A. N.; Tuchin, V. V. *Adv. Opt. Technol.* **2008**, *2008*, 1−8.
(11) Schulmerich, M. V.; Cole, J. H.; Dooley, K. A.; Morris, M. D.; Kreider, J. M.; Goldstein, S. A. *J. Biomed. Opt.* **2008**, *13* (2), 021108.
(12) Greenbaum, A.; Chan, K. Y.; Dobreva, T.; Brown, D.; Balani, D. H.; Boyce, R.; Kronenberg, H. M.; McBride, H. J.; Gradinaru, V. *Sci. Transl. Med.* **2017**, *9* (387), No. eaah6518.
(13) Zhao, Y. J.; Yu, T. T.; Zhang, C.; Li, Z.; Luo, Q. M.; Xu, T. H.; Zhu, D. *Light: Sci. Appl.* **2018**, *7*, 17153.
(14) Zhang, C.; Feng, W.; Zhao, Y. J.; Yu, T. T.; Li, P. C.; Xu, T. H.; Luo, Q. M.; Zhu, D. *Theranostics* **2018**, *8* (10), 2696−2708.
(15) Kim, J. H.; Jang, M. J.; Choi, J.; Lee, E.; Song, K. D.; Cho, J.; Kim, K. T.; Cha, H. J.; Sun, W. *Sci. Rep.* **2018**, *8*, 12815.
(16) Freudiger, C. W.; Min, W.; Saar, B. G.; Lu, S.; Holtom, G. R.; He, C. W.; Tsai, J. C.; Kang, J. X.; Xie, X. S. *Science* **2008**, *322* (5909), 1857−1861.
(17) Ozeki, Y.; Umemura, W.; Otsuka, Y.; Satoh, S.; Hashimoto, H.; Sumimura, K.; Nishizawa, N.; Fukui, K.; Itoh, K. *Nat. Photonics* **2012**, *6* (12), 845−850.
(18) Wei, M.; Shi, L.; Shen, Y.; Zhao, Z.; Guzman, A.; Kaufman, L. J.; Wei, L.; Min, W. *Proc. Natl. Acad. Sci. U. S. A.* **2019**, *116*, 6608−6617.
(19) Yang, Y. F.; Chen, L. C.; Ji, M. B. *J. Innovative Opt. Health Sci.* **2017**, *10* (2), 1730010−1730021.
(20) Buchwald, T.; Kozielski, M.; Szybowicz, M. *Spectroscopy* **2012**, *27*, 107−117.
(21) Yan, S.; Cui, S.; Ke, K.; Zhao, B.; Liu, X.; Yue, S.; Wang, P. *Anal. Chem.* **2018**, *90* (11), 6362−6366.
(22) Capitaine, E.; Moussa, N. O.; Louot, C.; Bardet, S. M.; Kano, H.; Duponchel, L.; Leveque, P.; Couderc, V.; Leproux, P. *Biomed. Opt. Express* **2018**, *9* (1), 245−253.
(23) Ando, M.; Liao, C. S.; Eckert, G. J.; Cheng, J. X. *J. Biomed. Opt.* **2018**, *23* (10), 105005.
(24) Wang, Z.; Zheng, W.; Hsu, C. Y. S.; Huang, Z. W. *Appl. Phys. Lett.* **2015**, *106* (3), 033701.
(25) Movasaghi, Z.; Rehman, S.; Rehman, I. U. *Appl. Spectrosc. Rev.* **2007**, *42* (5), 493−541.
(26) Sdobnov, A. Y.; Tuchin, V. V.; Lademann, J.; Darvin, M. E. *J. Phys. D: Appl. Phys.* **2017**, *50* (28), 285401.
(27) Crane, N. J.; Popescu, V.; Morris, M. D.; Steenhuis, P.; Ignelzi, M. A., Jr. *Bone* **2006**, *39* (3), 434−442.
(28) Tainaka, K.; Kuno, A.; Kubota, S. I.; Murakami, T.; Ueda, H. R. *Annu. Rev. Cell Dev. Biol.* **2016**, *32*, 713−741.
(29) Hua, L.; Zhou, R. H.; Thirumalai, D.; Berne, B. J. *Proc. Natl. Acad. Sci. U. S. A.* **2008**, *105* (44), 16928−16933.
(30) Scott, J. E.; Kyffin, T. W. *Biochem. J.* **1978**, *169* (3), 697−701.
(31) Hirshburg, J. M.; Ravikumar, K. M.; Hwang, W.; Yeh, A. T. *J. Biomed. Opt.* **2010**, *15* (5), 055002.
(32) Yang, B.; Treweek, J. B.; Kulkarni, R. P.; Deverman, B. E.; Chen, C. K.; Lubeck, E.; Shah, S.; Cai, L.; Gradinaru, V. *Cell* **2014**, *158* (4), 945−958.
(33) Richardson, D. S.; Lichtman, J. W. *Cell* **2015**, *162* (2), 246−257.
(34) Hama, H.; Kurokawa, H.; Kawano, H.; Ando, R.; Shimogori, T.; Noda, H.; Fukami, K.; Sakaue-Sawano, A.; Miyawaki, A. *Nat. Neurosci.* **2011**, *14* (11), 1481−1488.
(35) Hama, H.; Hioki, H.; Namiki, K.; Hoshida, T.; Kurokawa, H.; Ishidate, F.; Kaneko, T.; Akagi, T.; Saito, T.; Saido, T.; Miyawaki, A. *Nat. Neurosci.* **2015**, *18* (10), 1518−29.

DOI: 10.1021/acs.analchem.9b02624
Anal. Chem. 2019, 91, 9371−9375